Structure of a zosuquidar and UIC2-bound human-mouse chimeric ABCB1

Amer Alam[a], Raphael Küng[b], Julia Kowal[a], Robert A. McLeod[b], Nina Tremp[a], Eugenia V. Broude[c], Igor B. Roninson[c], Henning Stahlberg[b], and Kaspar P. Locher[a,1]

[a]Institute of Molecular Biology and Biophysics, ETH Zürich, 8093 Zürich, Switzerland; [b]Center for Cellular Imaging and NanoAnalytics, Biozentrum, University of Basel, 4058 Basel, Switzerland; and [c]Department of Drug Discovery and Biomedical Sciences, College of Pharmacy, University of South Carolina, Columbia, SC 29208

Edited by Douglas C. Rees, Howard Hughes Medical Institute and California Institute of Technology, Pasadena, CA, and approved January 19, 2018 (received for review September 28, 2017)

The multidrug transporter ABCB1 (P-glycoprotein) is an ATP-binding cassette transporter that has a key role in protecting tissues from toxic insult and contributes to multidrug extrusion from cancer cells. Here, we report the near-atomic resolution cryo-EM structure of nucleotide-free ABCB1 trapped by an engineered disulfide cross-link between the nucleotide-binding domains (NBDs) and bound to the antigen-binding fragment of the human-specific inhibitory antibody UIC2 and to the third-generation ABCB1 inhibitor zosuquidar. Our structure reveals the transporter in an occluded conformation with a central, enclosed, inhibitor-binding pocket lined by residues from all transmembrane (TM) helices of ABCB1. The pocket spans almost the entire width of the lipid membrane and is occupied exclusively by two closely interacting zosuquidar molecules. The external, conformational epitope facilitating UIC2 binding is also visualized, providing a basis for its inhibition of substrate efflux. Additional cryo-EM structures suggest concerted movement of TM helices from both halves of the transporters associated with closing the NBD gap, as well as zosuquidar binding. Our results define distinct recognition interfaces of ABCB1 inhibitory agents, which may be exploited for therapeutic purposes.

ABC transporter | structure | small-molecule inhibitors | cryo-EM | mechanism

P-glycoprotein (ABCB1) is an ATP-binding cassette transporter ubiquitously expressed in a wide range of cells and tissues, where it has an important role in cellular detoxification (1, 2). Its wide substrate specificity underlies its physiological relevance in drug transport across multiple blood–organ barriers, resulting in modulation of drug delivery, drug–drug interactions, and drug pharmacokinetics for a host of clinically active agents (1–4). ABCB1-mediated drug efflux has been linked to multidrug resistance, adversely affecting cancer chemotherapeutic treatment and treatment of various brain disorders (5–7). The ABCB1-specific inhibitory antibody UIC2 was developed with the goal of increasing antitumor drug treatment efficacy (8, 9). UIC2 targets the extracellular moiety of human ABCB1 ($ABCB1_H$) and has been successfully used to investigate the transport cycle of ABCB1 owing to its ability to bind the transporter during various states of the catalytic cycle (9–11). Although the crystal structure of the antigen-binding fragment (Fab) of UIC2 has been determined (12), the conformational epitope on the surface of $ABCB1_H$ has remained elusive because direct visualization of the ABCB1–UIC2 interface was limited to low-resolution cryo-EM reconstructions (13). To date, several structures of mouse ABCB1 are available, including those with bound inhibitors (14–17) and nucleotides (18). However, despite added ligands, all these reveal the transporter in an inward-open conformation with varying degrees of nucleotide-binding domain (NBD) separation and a largely unchanged transmembrane domain (TMD) and substrate translocation pathway.

Small-molecule, third-generation inhibitors, including zosuquidar, tariquidar, and elacridar (19–21), have shown potential in model systems for coadministration with various anticancer agents. However, antibody- and small-molecule inhibitor–based strategies have not been successfully utilized clinically (22, 23), emphasizing the need for designing more effective therapeutic and diagnostic strategies targeting ABCB1 expression and inhibition. A detailed understanding of the structure of ABCB1 with bound antibody fragments and drugs/inhibitors in different conformations is central to improving the specificity of inhibitors and to further our understanding of the chemistry governing ABCB1 interaction with high-potency inhibitors. To achieve this, we generated a hybrid construct of human and mouse ABCB1 ($ABCB1_{HM}$) that contains the extracellular region of the human protein, including the recognition epitope of UIC2, on a background of mouse ABCB1. $ABCB1_{HM}$ shares ∼90% sequence identity with the human protein (*SI Appendix*, Fig. S1) and takes advantage of the higher biochemical stability of mouse ABCB1, which shares high sequence similarity and, except for subtle differences, exhibits highly similar substrate/inhibitor-binding properties with its human homolog, especially with regard to third-generation inhibitors (24). As highlighted in Fig. 1 and *SI Appendix*, Fig. S1, our results reveal key $ABCB1_H$-specific residues involved in the interaction interfaces of both zosuquidar and UIC2 and ABCB1.

ABCB1 has been observed to exist in a range of conformations with varying degrees of NBD separation, including a nucleotide-

Significance

The ATP binding cassette transporter ABCB1 (also termed P-glycoprotein) is a physiologically essential multidrug efflux transporter of key relevance to biomedicine. Here, we report the conformational trapping and structural analysis of ABCB1 in complex with the antigen-binding fragment of UIC2, a human ABCB1-specific inhibitory antibody, and zosuquidar, a third-generation ABCB1 inhibitor. The structures outline key features underlining specific ABCB1 inhibition by antibodies and small molecules, including a dual mode of inhibitor binding in a fully occluded ABCB1 cavity. Finally, our analysis sheds light on the conformational transitions undergone by the transporter to reach the inhibitor-bound state.

Author contributions: A.A. and K.P.L. designed research; A.A., R.K., J.K., N.T., E.V.B., and H.S. performed research; E.V.B. and I.B.R. contributed new reagents/analytic tools; A.A., R.K., J.K., R.A.M., I.B.R., H.S., and K.P.L. analyzed data; and A.A. and K.P.L. wrote the paper.

The authors declare no conflict of interest.

This article is a PNAS Direct Submission.

Data deposition: Data associated with this paper have been deposited in the Electron Microscopy Data Bank (EMDB) (accession nos. EMD-4281–EMD-4285). Coordinate data have been deposited to the Research Collaboratory for Structural Bioinformatics (PDB accession nos. 6FN1 and 6FN4).

[1]To whom correspondence should be addressed. Email: locher@mol.biol.ethz.ch.

This article contains supporting information online at www.pnas.org/lookup/suppl/doi:10.1073/pnas.1717044115/-/DCSupplemental.

Published online February 13, 2018.

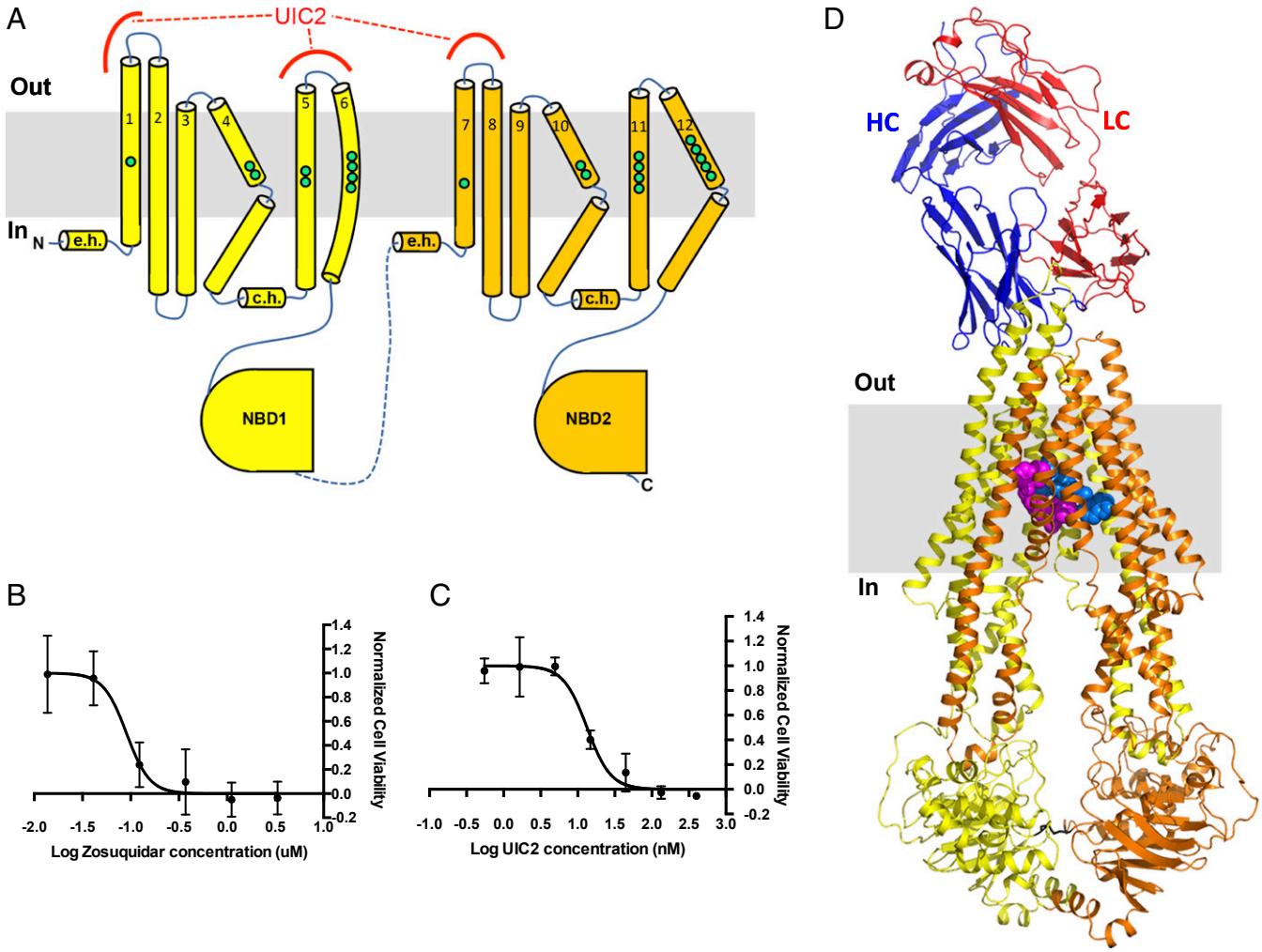

Fig. 1. Structural and functional characterization of UIC2-Fab and zosuquidar-bound ABCB1. (*A*) Topology diagram of ABCB1. TM helices are numbered, and their relative lengths, as well as the locations of kinks or bends, are schematically illustrated. The locations of residues interacting with bound zosuquidar are schematically shown as filled green circles. External loops EL1, EL3, and EL4 interact with bound UIC2-Fab, as indicated by red lines. C, carboxy terminus; c.h., coupling helices; e.h., elbow helices; N, amino terminus. (*B*) Inhibition of $ABCB1_{HM\text{-}X}$–mediated protection from paclitaxel by zosuquidar ($n = 3$, error bars represent SD). (*C*) Inhibition of $ABCB1_{HM\text{-}X}$–mediated protection from paclitaxel by UIC2 ($n = 3$, error bars represent SD). (*D*) Ribbon representation of the UIC2-bound $ABCB1_{HM\text{-}X}$ structure, with the two halves of ABCB1 colored yellow and orange, respectively, and the heavy (HC) and light (LC) chains of UIC2-Fab colored blue and red, respectively. The approximate location of the membrane is depicted in gray. Two bound zosuquidar molecules are shown in light blue and pink sphere representation. The engineered disulfide between the two NBDs is shown as black sticks.

bound "closed" conformation, where no gap between NBDs exists (13). To understand its interaction with small molecules, we sought to visualize an intermediate conformation of the transporter, where the NBD gap has been partially, but not fully, closed. To visualize and analyze the effect of progressive NBD gap closure on the TMD domains (in the absence of bound nucleotides in this case), we therefore generated a variant that allowed disulfide cross-linking of the NBDs of the transporter ($ABCB1_{HM\text{-}X}$). The latter harbors two S → C mutations at positions 559 and 1,204 in the dimerization (D)-loops, expected to come within close proximity to each other upon NBD dimerization as seen in the canonical ABC exporter Sav1866, among others, and successfully used for conformational trapping and high-resolution analysis of other ABC transporters (25, 26).

Results

Conformational Trapping and Functional Characterization of $ABCB1_{HM}$. $ABCB1_{HM\text{-}X}$ was shown in vivo to confer up to 50-fold higher paclitaxel resistance to mammalian cells when expressed in an inducible HEK293 cell line compared with uninduced cells (*SI Appendix*, Fig. S2*A*), showing that the construct retains paclitaxel transport activity. The construct is strongly inhibited by zosuquidar and UIC2, which resensitize $ABCB1_{HM\text{-}X}$–expressing cells to paclitaxel (Fig. 1 *B* and *C*) at nanomolar concentrations. The constructs were expressed in HEK293 cells and purified in a lauryl maltose neopentyl glycol (LMNG) and cholesteryl hemisuccinate (CHS) mixture in contrast to the more commonly used dodecyl maltoside (DDM)-based preparations to avoid interference from nonspecifically bound DDM molecules in the transmembrane (TM) ligand-binding cavity. Disulfide cross-linking of $ABCB1_{HM\text{-}X}$ was nearly complete in the absence of added nucleotides, as revealed by gel electrophoresis (*SI Appendix*, Fig. S2*B*), and $ABCB1_{H}$, $ABCB1_{HM}$, and cross-linked or reduced $ABCB1_{HM\text{-}X}$ all showed near-identical UIC2-binding affinities (*SI Appendix*, Fig. S2*C*).

While previous studies have reported negligible basal ATPase rates for detergent-purified ABCB1 (27), our LMNG/CHS-purified $ABCB1_{H}$ and $ABCB1_{HM}$ constructs maintain a measurable, albeit low, basal ATPase rate (~20–30 nmol·min^{-1}·mg^{-1}), which is stimulated up to 10-fold by addition of zosuquidar or the

anticancer drug paclitaxel (*SI Appendix*, Fig. S2*D*), allowing for characterization of drug-mediated ATPase activity in an identical environment as used for our structural analysis. Although disulfide cross-linking did not alter K_m values for ATP hydrolysis in $ABCB1_{HM\text{-}X}$ and its ATPase stimulation by zosuquidar, we observed a reduction in ATPase stimulation by paclitaxel that could be reversed by addition of DTT (*SI Appendix*, Fig. S2 *D* and *E*). Interestingly, zosuquidar has been shown to stimulate the ATPase rate of detergent (DDM)-solubilized ABCB1 but inhibits the lipid-reconstituted ABCB1 ATPase rate, with the effect in the latter being much stronger (EC_{50} ~ 200 nM, roughly 50-fold lower than that obtained in DDM micelles) (24). This opposing effect in detergent versus lipid has been speculated to stem from the occlusion of a primary high-affinity zosuquidar-binding site by DDM molecules, leading to zosuquidar binding to a secondary low-affinity site. As seen in *SI Appendix*, Fig. S2*F*, while the ATPase activity of both $ABCB1_H$ and $ABCB1_{HM}$ purified in LMNG/CHS is stimulated by zosuquidar, the EC_{50} values for this modulation are ~200 nM, comparable to those reported for native membranes. Combined with the absence of bound detergent molecules in our inhibitor-bound structure, our results suggest that zosuquidar is bound to its primary site in our studies, as explained below.

Overall Structure of ABCB1–UIC2 in Complex with Zosuquidar. The structure of cross-linked, zosuquidar-bound $ABCB1_{HM\text{-}X}$ was solved to an overall resolution of 3.58 Å [Fourier shell correlation (FSC) cutoff of 0.143] (Fig. 1*D* and *SI Appendix*, Fig. S3). The high disulfide trapping efficiency correlated well with the observation that the overwhelming majority of usable particles corresponded to a single conformation of ABCB1. The local resolution was highest in the TM region, allowing unambiguous de novo building of the TMDs, including the zosuquidar-binding pocket, as well as the ABCB1–UIC2 interface (*SI Appendix*, Fig. S4). Despite their close association due to the disulfide cross-link, the NBDs did not adopt a fully closed sandwich conformation, which is a hallmark of ATP-bound structures, because no nucleotide was added. They maintained a degree of conformational flexibility reflected in the lower resolution of the electron density, nevertheless allowing atomic interpretation guided by the structures of mouse ABCB1 previously reported with minor manual adjustment where appropriate. Despite the overall lower resolution for the NBDs, density for the introduced disulfide cross-link was visible. The NBD arrangement was somewhat asymmetrical, closely matching that observed in the heterodimeric, bacterial homolog of ABCB1, TM287/288 (28). Asymmetry in ABCB1 hydrolysis has previously been proposed (18, 29) and also observed in a bacterial homolog of asymmetrical B family transporters, TmrAB (30). Our structure revealed a single copy of UIC2-Fab bound to the external side of the transporter and tilted by about 70° relative to the membrane plane (Fig. 1*D*). Whereas the architecture and fold of $ABCB1_{HM}$ are similar to those of mouse ABCB1 (15, 18), the trapped conformation is distinct from previous structures because the NBDs are closer together and the TMDs assume a conformation that provides structural insight into an occluded and inhibitor-bound state of a B-family ABC exporter. As with previously reported ABCB1 structures, no density was observed for the linker region connecting the two halves of the transporter.

Molecular Details of the ABCB1–UIC2-Binding Interface. UIC2 recognizes a conformational epitope of ABCB1 that involves residues from TM1 and TM2 and the extracellular loops EL1, EL3, and EL4 (Fig. 2 *A* and *B*), in agreement with biochemical studies that have identified the external part of TM1 (8) and the external loop connecting TM5 and TM6 (EL3) (11) as contributing to the $ABCB1_H$–UIC2 interface. The buried surface area amounts to ~1,075 $Å^2$, with the heavy chain of UIC2-Fab forming the bulk of the interface (~80%). The observed interactions include polar, electrostatic, and hydrophobic contacts, including methionine-pi stacking. Differences in the amino acid sequences of the external loops of $ABCB1_{HM}$ can readily explain the specificity of UIC2 for the human protein over that of rodents (Fig. 2*C*). Additionally, the observed interaction provides a structural explanation of how UIC2 inhibits transport activity of ABCB1: By clamping the external loops together, UIC2 prevents ABCB1 from converting to an outward-open conformation, which is required to release substrate to the outside (31, 32). This is in line with studies indicating incomplete UIC2 binding in unmodified ABCB1-expressing cells (8), where the transporter is expected to exist in a mixture of conformations, including a UIC2-incompatible, outward-open state. It also agrees with the observed modulation of UIC2 affinity for ABCB1 in the presence or absence of various nucleotides and substrates (11). Any alteration of the equilibrium between the outward-open and outward-closed conformations of ABCB1 caused by the binding or release of drugs/nucleotides as part of the transporter's catalytic cycle could alter its affinity for UIC2. As ABCB1 has previously been shown to hydrolyze ATP in the presence of UIC2 (33), we conclude that the architecture of ABCB1 allows the NBDs to bind and hydrolyze ATP, while having the TMDs assume an outward-closed conformation. This is in agreement with the expected conformational landscape sampled by ABCB1 based on recent spectroscopic measurements and molecular dynamics studies on mouse ABCB1 (31), where an outward-occluded state with a closed NBD interface and outward closed TMD has been observed. Such a conformation is also compatible with those observed in structures of related prokaryotic ABC exporters (28, 34), as well as the recently determined ATP-bound zebrafish CFTR structure (35), and is expected to be generally shared among various ABC exporter family members (36).

Details of the Zosuquidar-Binding Pocket. The zosuquidar-bound structure of ABCB1 reveals a large cavity that spans almost the entire width of the lipid membrane (Figs. 1*D* and 2 *D* and *E*). The cavity is sealed from the external and cytoplasmic sides, and is lined by residues from all 12 TMs of ABCB1 (Fig. 1*A* and *SI Appendix*, Fig. S1), comprising many of the residues identified in biochemical studies as contributing to drug interactions of ABCB1 (37–42). Although some of these side chains have been observed to be in contact with ligands in previously reported structures of ABCB1, these structures all described inward-facing conformations, with no enclosed cavities observed and fewer interactions with bound substrates (14, 15, 17, 43). As shown in Fig. 2 *D* and *E*, our EM density unambiguously revealed two zosuquidar molecules bound in the enclosed cavity, filling most, but not all of the available space. As a consequence, residues from eight TMs directly interact with bound zosuquidar. The two zosuquidar molecules assume defined orientations, are wrapped around each other, and roughly follow a twofold rotational symmetry. This is in stark contrast to structures of mouse ABCB1 in complex with cyclic inhibitors in the inward-open conformation (43). The distribution of interacting residues, which are fully conserved between our construct and $ABCB1_H$ (green dots in Fig. 1*B* and *SI Appendix*, Fig. S1), demonstrates that the two halves of ABCB1 contribute in a pseudosymmetrical fashion to zosuquidar binding, as the contacting residues belong to TM1, TM4, TM5, and TM6 (first half of ABCB1) and to TM7, TM10, TM11, and TM12 (second half of ABCB1). In addition to the many aromatic and hydrophobic residues, there are polar or charged side chains in the observed cavity (*SI Appendix*, Fig. S5). The majority of these have been predicted to be part of the primary drug-binding site of ABCB1 (15, 40, 41, 44). Specifically, Y953 is seen in our structure to hydrogen-bond with one of the zosuquidar molecules (*SI Appendix*, Fig. S6*B*) as predicted based on molecular dynamics and mutagenesis studies, although this study predicted

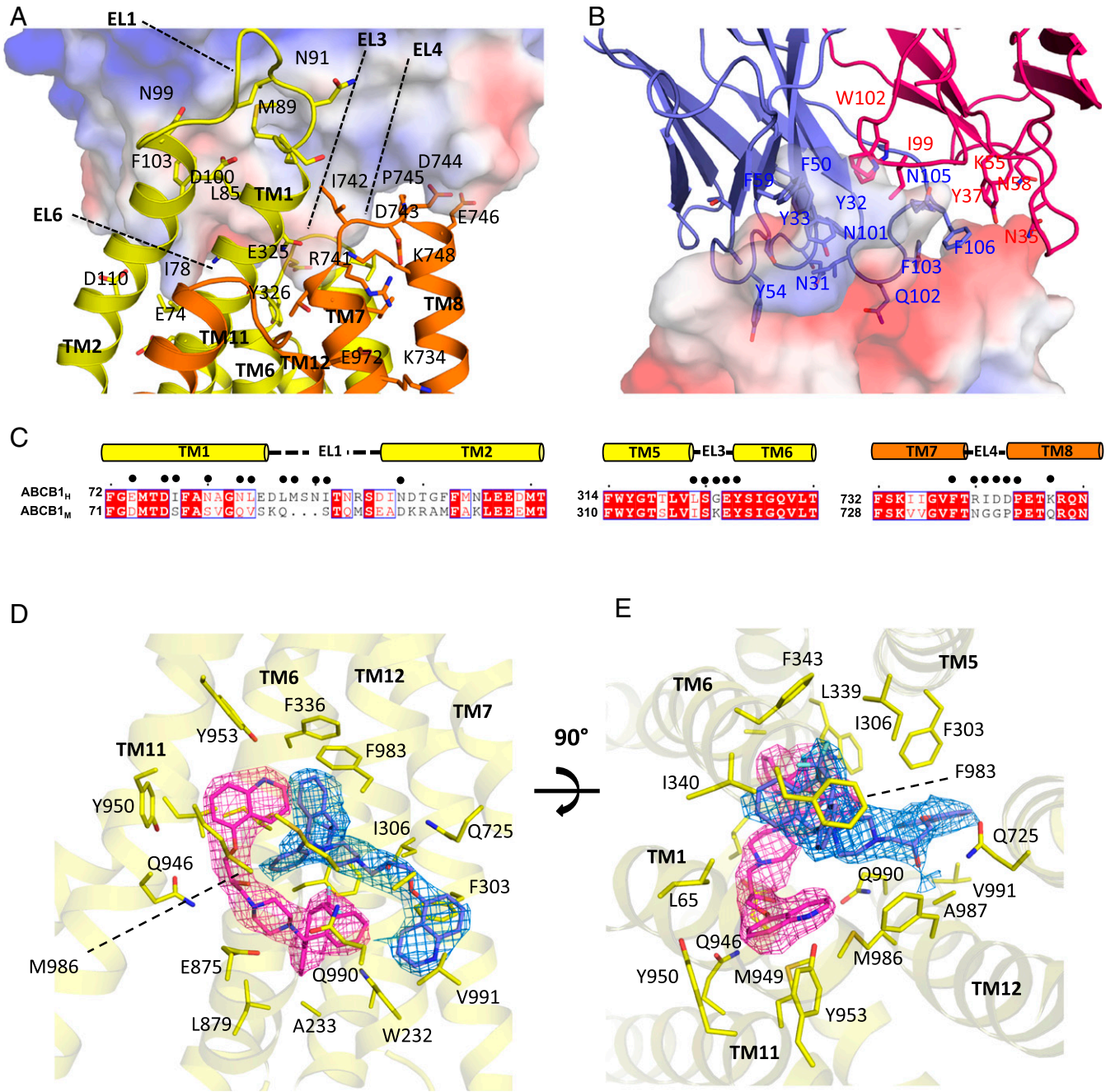

Fig. 2. Details of UIC2-binding interface and zosuquidar-binding pocket. (*A*) Close-up view of the ABCB1–UIC2 interface with the UIC2-Fab–binding region shown as an electrostatic surface potential map and ABCB1 shown in ribbon representation. TM helices and ELs of ABCB1 are labeled. ABCB1 residues interacting with UIC2-Fab or with a structural role in stabilizing the outward-closed conformation of ABCB1 are shown as sticks and labeled. (*B*) Similar view as in *A*, but with ABCB1 shown as semitransparent electrostatic surface potential map. UIC2-Fab is shown in ribbon representation and colored blue (heavy chain) or red (light chain). Select UIC2 residues within 5 Å of ABCB1 are shown as sticks. (*C*) Sequence alignments of EL1, EL3, and EL4 regions of $ABCB1_H$ and mouse ABCB1, with secondary structure motifs shown above the sequences. Black dots represent residues of $ABCB1_H$ within 4 Å of UIC2 as seen in our $ABCB1_{HM\text{-}X}$–UIC2 structure. (*D*) Ribbon diagram of ABCB1 viewed parallel to the membrane plane, with several TM helices removed for clarity. Two bound zosuquidar molecules are shown as pink and blue sticks, and the corresponding EM density is shown as pink and blue mesh. Selected ABCB1 residues within 4 Å distance of bound zosuquidar are shown as yellow sticks and labeled. (*E*) Similar to *D* but viewed from the external side of the membrane.

only one zosuquidar bound in the cavity in a different configuration compared with that observed in our structure. The absence of interfering detergent, along with the close association of the bound inhibitors with residues predicted to be primary contributors to specific binding of zosuquidar (37), further validates the relevance of the observed binding site. The observation of two bound zosuquidar molecules agrees with previous biochemical and structural findings suggesting that the ABCB1 drug-binding pocket is capable of accommodating multiple ligands simultaneously (43, 45). The presence of many aromatic residues can offer an adaptive plasticity to the pocket, in line with studies suggesting an induced fit mechanism of ligand recognition (46). We conclude that ABCB1 may bind inhibitors through a combination of specific interactions, leading to defined

binding modes and a rigid core of bound inhibitor molecules surrounded by TM helices.

Conformational Changes Associated with NBD Closure. To understand the contributions of disulfide-mediated NBD trapping and zosuquidar binding to the TMD conformation and the formation of an inhibitor-binding pocket, we determined two additional cryo-EM structures (Fig. 3*A*). The structure of an amphipol (A8-34) reconstituted, non–cross-linked variant, $ABCB1_{HM\text{-}EQ}$, was determined in the absence of any drugs or nucleotides, but in complex with UIC2-Fab (*SI Appendix*, Fig. S6). $ABCB1_{HM\text{-}EQ}$ harbors an E → Q mutation in the Walker-B motif, which increases the stability and limits the conformational heterogeneity of the sample. The $ABCB1_{HM\text{-}EQ}$ structure revealed an inward-open conformation with wide NBD separation, closely matching (rmsd = 1.88 for all aligned Cα atoms) previously reported mouse ABCB1 structures (15, 16, 18, 43) (*SI Appendix*, Fig. S6*E*). A detailed structural analysis (Fig. 3*B*) revealed that the transition from the inward-open state to the disulfide-trapped, zosuquidar-occluded state includes distinct changes in the TMDs, most significantly in the conformations of TM4 and TM10 (Fig. 3*C*). Despite exhibiting different sequences otherwise, the three residues P223, S238, and G251 in TM4 correspond to identically spaced and located residues P866, S880, and G894 in TM10, allowing for similar helix bending and kinking. Along with the already bent and kinked TM6 and TM12, this amounts to four TM helices of ABCB1 that form significant kinks, forming a cytoplasmic gate to the zosuquidar-binding cavity and closing the lateral membrane opening that exists in the inward-open conformation (Fig. 4 *A* and *B*). We then determined the structure of disulfide-trapped $ABCB1_{HM\text{-}X}$, also in complex with UIC2-Fab, but in the absence of drugs or nucleotides. We found that the separation of the

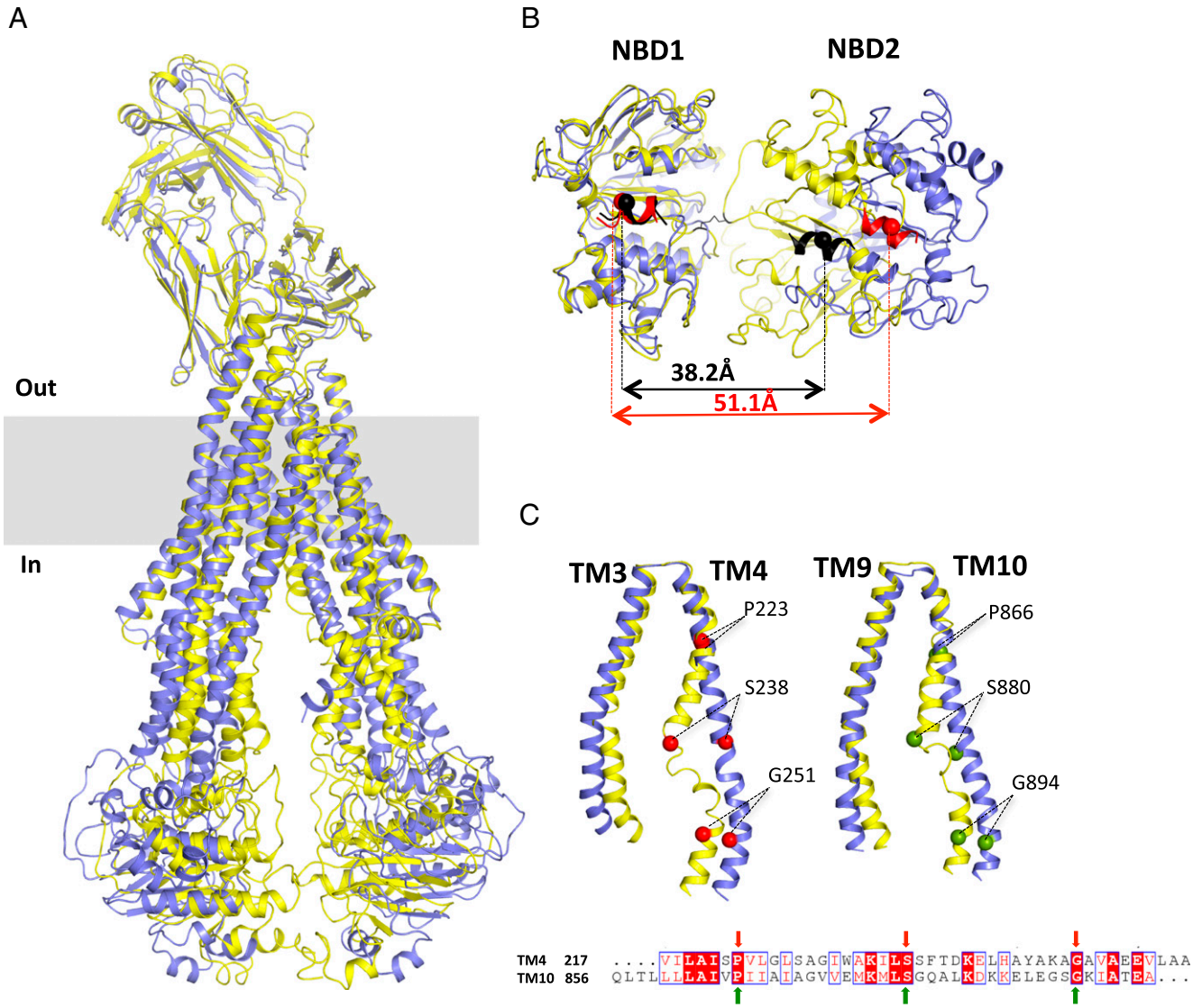

Fig. 3. Conformational changes in ABCB1. (*A*) Comparison of apo-inward $ABCB1_{HM}$–UIC2 (blue) and disulfide-trapped, apo $ABCB1_{HM\text{-}X}$–UIC2 (yellow) using UIC2-Fab as an anchor point for the superposition. The gray box represents the approximate location of the plasma membrane. (*B*) Close-up view of the NBDs of the two structures shown in *A*, but using NBD1 as the superposition anchor. The coupling helices of $ABCB1_{HM}$ and $ABCB1_{HM\text{-}X}$ are colored red and black, respectively. The Cα atoms of V264 and V908 of the coupling helices are represented as spheres, with the distance between them shown as black and red arrows. (*C*) Superposition of the TM helix pairs TM3–TM4 and TM9–TM10 of the two ABCB1 structures colored as in *A*. Red and green spheres depict Cα atoms of selected residues, with numbers indicated. A sequence alignment of TM4 and TM10 of human ABCB1 is shown below the structures, and the designated residues are indicated with arrows.

NBDs in the apo $ABCB1_{HM-X}$ structure was identical to that of the zosuquidar-bound state. The conformation of the external loops of ABCB1 and the conformation of the interface with UIC2 binding are indistinguishable in the three structures, which is in line with the observation that UIC2 binding allows the transporter to cycle through its complete ATP hydrolysis cycle despite the absence of a discrete outward-open conformation (13, 33). Although the structure of disulfide-trapped apo $ABCB1_{HM-X}$ is at slightly lower resolution than the zosuquidar-bound structure, side-chain density is still visible for most TMs, allowing unambiguous determination of the side-chain register. When all particles are used for 3D reconstruction, we observed blurred density in the regions of TM4 (residues 237–244) and TM10 (residues 880–888) owing to local conformational flexibility (*SI Appendix*, Figs. S7–S9). Upon subclassifying, we could identify distinct and roughly equally populated conformations where TM4 and TM10 either adopt kinked conformations (class 1/map 2) as observed in the zosuquidar-bound state (Fig. 4*C*) or straight conformations (class 2/map 3) as observed in the apo-inward $ABCB1_{HM}$ structure. We conclude that the closing of the NBD gap by disulfide trapping, which is transmitted to the TMDs via the coupling helices, allows TM4 and TM10 to sample both the straight and kinked conformations. Upon binding of zosuquidar, only the kinked conformation is observed. A stabilization of the two TMDs of ABCB1 has been also been reported upon binding of the third-generation ABCB1 inhibitor tarquidar (38), whose proposed binding site overlaps with the zosuquidar-binding site in our structure, pointing to similar modes of interaction with the transporter. In the related multidrug transporter ABCC1/MRP1 (47), binding of substrate was accompanied by a slight reduction in NBD separation and narrowing of the binding pocket, which, nevertheless, remained open to the cytoplasm.

Conclusions

Our results provide a number of insights into the modulation of ABCB1, as well as the chemistry of the underlying specific ligand interactions. First, we offer visualization of a fully occluded ligand-binding cavity of a type 1 ABC transporter occupied by a small-molecule inhibitor, identifying the details of zosuquidar binding to ABCB1. Such a conformation has been extremely difficult to trap owing to the highly dynamic nature of ABCB1, prompting us to employ covalent linkage of the NBDs. Given that disulfide-trapped $ABCB1_{HM-X}$ hydrolyzes ATP at a similar rate as the native protein and maintains stimulation by zosuquidar, the observed conformation provides physiologically relevant insight. This is further supported by the fact that we observed spontaneous and near-complete cross-linking for the designed cysteine pairs, and our structural analysis revealed the majority of particles to belong to a homogeneous class, consistent with an occluded state of ABCB1. Visualization of an occluded ABCB1 cavity offers a unique tool for in silico studies of drug binding to the transporter, which have so far relied on inward-open structures of ABCB1 and models based on different transporters. The ability of two inhibitor molecules to bind in tandem raises the possibility of cooperativity in binding, which, in the absence of a more sensitive readout for drug binding, we are currently unable to fully analyze. The zosuquidar-inhibited state captured in our structure also raises the question of whether transport substrates can bind similarly in well-defined orientations to the exact same site in ABCB1. Interestingly, based largely on its opposing ATPase

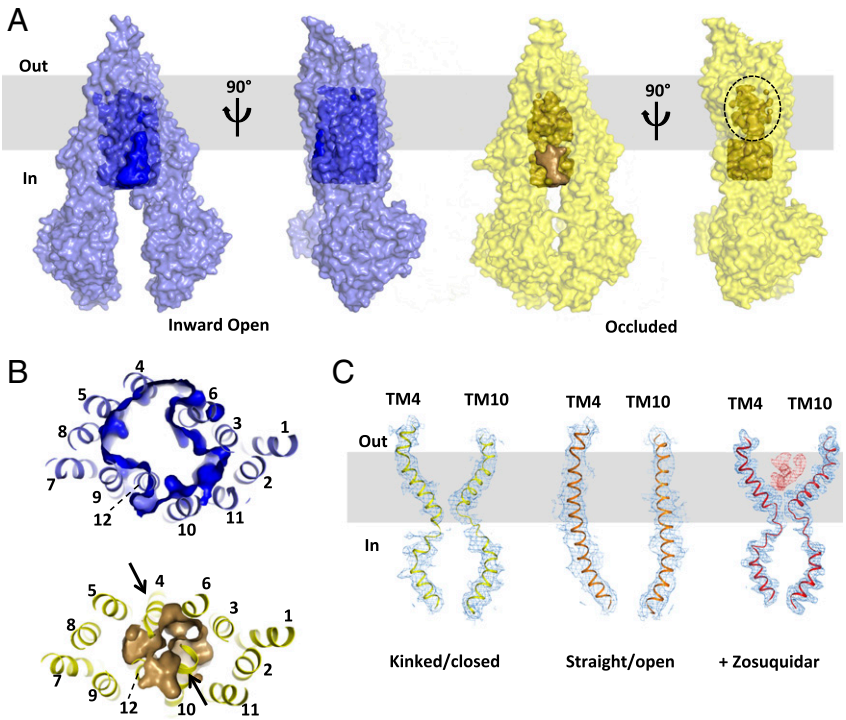

Fig. 4. Structural changes in the translocation pathway. (*A*) Surface representations of inward-open $ABCB1_{HM}$ and disulfide-trapped $ABCB1_{HM-X}$ structures (without bound UIC2-Fab) colored blue and yellow, respectively. Internal cavity volumes are depicted as dark blue and gold-colored surfaces. The dashed oval indicates the location of the occluded TM cavity that binds zosuquidar in the zosuquidar-bound structure. The gray box represents the membrane. (*B*) Translocation pathways of $ABCB1_{HM}$ and $ABCB1_{HM-X}$ colored as in *A*, but viewed from the cytoplasmic side of the membrane. TM helices are shown as ribbons and numbered. Arrows indicate the constriction point or cavity gate formed by kinks in TM4 and TM10, closing off the cavity to the cytoplasm in the occluded $ABCB1_{HM-X}$ structure. (*C*) Side views of ribbon representation of TM4 and TM10 and the corresponding EM density of $ABCB1_{HM-X}$ structures. (*Left* and *Center*) Two populations of disulfide-trapped apo $ABCB1_{HM-X}$, suggesting equilibrium between kinked (closed) and straight (open) conformations. (*Right*) Zosuquidar-bound structure, where only the kinked conformation exists. Density for the bound zosuquidar molecules is shown as red mesh.

modulatory behavior in lipid- or detergent-embedded ABCB1, zosuquidar, along with elacridar and tariquidar, has recently been proposed to bind to a low-affinity site in the presence of detergent, which is thought to bind to, and hence render, the proposed high-affinity site inaccessible for the inhibitor (24). While we cannot categorically rule out such a different binding mode for zosuquidar, a number of observations help further validate the physiological relevance and significance of our zosuquidar-bound structure. First, we observe no interfering detergent molecules in the binding cavity, arguing against detergent-mediated occlusion of the primary zosuquidar-binding site. Second, our EC_{50} values for zosuquidar modulation of LMNG-solubilized ABCB1 match those measured in native membranes, with our observed modulation effect being much stronger than that reported for DDM-based preparations (24). Third, the conformational changes in TM4 and TM10, although never before seen to occur in tandem, closely match those observed for TM4 in mouse ABCB1 in complex with select cyclic peptide inhibitors (43). In light of these findings, the explanation for the opposing effects of zosuquidar on ATPase activity of lipid-reconstituted or detergent-solubilized ABCB1 may need to be readdressed.

Second, the ability to narrow the NBD gap by cross-linking rather than addition of nucleotides allowed for the intriguing finding of abrogated ATPase stimulation by paclitaxel. While subtle conformational changes within the observed occluded cavity upon full NBD closure with bound nucleotides are possible, this result might indicate that some transport substrates (including paclitaxel) cannot access the occluded conformation seen in our zosuquidar-bound structure. Although individual instances of helix bending/kinking have previously been observed in ABCB1 structures (16, 43, 48), our structures visualize simultaneous conformational changes in the two halves of the transporter, involving conserved, helix-breaking residues. The structural rearrangements in the TMDs may not only occur during inhibition but possibly also during a productive transport cycle.

Finally, we elucidate the conformational epitope of the UIC2 antibody and the mechanism of its inhibitory activity. Most importantly, our structure clearly rules out the existence of an outward-open ABCB1 conformation in the presence of UIC2 as speculated upon based on low-resolution EM analysis of human ABCB1–UIC2 complexes (13).

Overall, the work presented herein opens new avenues for the development of more potent antibody and small-molecule inhibitors of ABCB1 that could be used alone or in combination with small-molecule inhibitors, while shedding light on the conformational changes undergone by the transporter upon ligand binding.

Materials and Methods

Protein Expression and Purification. A PCR-free cloning strategy was employed for all $ABCB1_{HM}$ constructs, which were synthetically generated (Thermo Fisher Scientific). For the variant of the $ABCB1_{HM}$ D-loop cross-link mutant ($ABCB1_{HM\text{-}X}$), a 3C protease site (LEVLFQGP) replaced residues 668–675 in the linker connecting the two halves of the transporter. All genes were cloned into an expression vector harboring the pXLG gene expression cassette in a pUC57 vector (GenScript) (49, 50) between BamH1 and Not1 restriction digestion sites. All genes were cloned with a C-terminal EYFP/rho-ID4 tag with an intervening precision (3C) protease cleavage site between the protein and purification tag. A stable cell line for $ABCB1_{HM\text{-}X}$ was generated using the Flp-In T-REx Kit (Thermo Fisher Scientific) for inducible expression as per the manufacturer's guidelines.

Transient expression for $ABCB1_{HM}$ and $ABCB1_{H}$ (sequence ID AAA59576.1) constructs was carried out in HEK293T adherent cultures. Cells were grown and maintained in DMEM (Thermo Fisher Scientific) supplemented with 10% FBS (Thermo Fisher Scientific) at 37 °C with 5% CO_2 under humidified conditions. Purified DNA was mixed with branched polyethylenimine (PEI; Sigma) at a 1:2 (DNA/PEI) ratio and applied to cells after exchanging medium to expression medium (DMEM + 2% FBS). Expression and growth media were supplemented with a penicillin/streptomycin mixture (Thermo Fisher Scientific). For $ABCB1_{H}$, expression was allowed to proceed for 72 h at 37 °C. All synthetic gene constructs were expressed in the presence of 4 mM valproic acid (Sigma) at 30 °C for 96 h. A stable cell line for $ABCB1_{HM\text{-}X}$ was grown and maintained similarly; induced with 1 $\mu g \cdot mL^{-1}$ tetracycline and protein expression, it was allowed to proceed for 72 h at 37 °C. Cells were washed with PBS before being harvested and flash-frozen in liquid nitrogen for storage at −80 °C.

For protein purification, frozen cell pellets were thawed and homogenized using a Dounce homogenizer in an eightfold (vol/wt) excess of resuspension buffer containing 150 mM NaCl and 25 mM Hepes (pH 7.5), in addition to 10–20% glycerol and a protease inhibitor mix (prepstatin A, leupeptin, soy trypsin inhibitor, and phenylmethylsulfonyl fluoride), followed by addition of detergent, except for the $ABCB1_{HM\text{-}EQ}$ sample for EM analysis, which was purified in 250 mM NaCl and 50 mM Tris (pH 7.5). For all $ABCB1_{H}$ genes, protein extraction was allowed to proceed in the presence of a mixture of 0.4% dodecyl maltopyranoside (DDM), 0.1% octaethylene glycol monododecyl ether (C12E8), and 0.1% CHS for 90 min before being centrifuged for 30 min at 37,060 × *g* in a SA600 fixed-angle rotor. For $ABCB1_{HM}$ constructs, 0.5/0.05% LMNG/CHS was used for solubilizing protein for 60 min before centrifugation. Clarified supernatant was applied to Sepharose-coupled Rho-ID4 antibody (University of British Columbia) and incubated for 3–18 h. Beads were washed four times with 10 column volumes (CV) of purification buffer containing 150 mM NaCl, 25 mM, and Hepes (pH 7.5), along with 10–20% glycerol and 0.01/0.01/0.004% DDM/C12E8/CHS ($ABCB1_{H}$) or 0.02/0.004% LMNG/CHS (all $ABCB1_{HM}$ constructs). For the $ABCB1_{HM\text{-}EQ}$ sample for EM analysis, buffer and salt components were adjusted to contain 250 mM NaCl and 20 mM Tris (pH 8.0). For direct comparison of $ABCB1_{H}$ and $ABCB1_{HM}$ constructs in ATPase assays, DDM/C12E8/CHS-solubilized $ABCB1_{H}$ was bound to ID4 columns and exchanged to LMNG/CHS buffer during the wash and subsequent purification steps. Protein was eluted by adding 3 CV of wash buffer containing a 1:10 wt/wt excess of 3C protease or by addition of 0.5 mg/mL ID4 peptide (GenScript) for 2–18 h. The 3C protease was His-tagged and removed by incubating the cleaved protein with nickel nitrilotriacetic acid beads (Qiagen). All purification steps were carried out at 4 °C.

Antibody Purification and Fragmentation. UIC2 hybridoma cells were cultured in Wheaton CeLLine Bioreactors as per the manufacturer's recommendations. Protein G and Protein A (GenScript) columns were used for antibody purification and antibody fragmentation, which were carried out using the Fab Preparation Kit protocol (Thermo Fisher Scientific). Fab purity was judged by SDS/PAGE, followed by size exclusion chromatography (SEC), after desalting into storage buffer containing 150 mM NaCl and 25 mM Hepes (pH 7.5) or 250 mM NaCl and 20 mM Tris (pH 8.0) for use with $ABCB1_{HM\text{-}EQ}$ for EM analysis.

Cytotoxicity Assays. The $ABCB1_{HM\text{-}X}$ stable cell line was grown and maintained as described above. Induced or noninduced cells were plated at a density of 5,000–10,000 cells per well of a 96-well plate and allowed to attach for 1–2 h. Cells were then exchanged to medium containing paclitaxel at various concentrations and incubated for a further 48–72 h. Medium was exchanged, and cell viability was measured using the WST-1 cell proliferation/viability kit (Sigma). The assay was repeated in the presence of 10 μM zosuquidar, added 1–3 h before paclitaxel. To test the effect of UIC2, induced cells were plated as described above and preincubated with varying UIC2 concentrations for 1 h at 37 °C. Paclitaxel was then added directly to the medium (final concentration 0.5 μM), cells were incubated for 48–72 h, and viability was measured described as above. The results shown are for three independent experiments (Fig. 1 *B* and *C* and *SI Appendix*, Fig. 2*A*). Data were fit to a sigmoidal dose–response curve, plotted in GraphPad Prism 6, and normalized to calculated B_{max} values from the fitted curve after subtraction of the calculated B_{min} values (to adjust for background levels in separate assays) from the respective datasets.

Cysteine Cross-Linking of $ABCB1_{HM\text{-}X}$. Detergent-purified protein was incubated with 1 mM dichloro(1,10-phenanthroline)copper(II) (Sigma) for 1 h at 4 °C and desalted back into buffer lacking the oxidant using Sephadex G-25 desalting columns (GE Healthcare) to stop the reaction. For $ABCB1_{HM\text{-}X\text{-}3C}$, cross-linking efficiency was analyzed by SDS/PAGE (*SI Appendix*, Fig. S2*B*). The 3C protease-cleaved samples were loaded in reducing and nonreducing loading buffer, and the ratio of cross-linked to non–cross-linked transporter was judged by comparing the full transporter band (cross-linked, ~140 kDa) and the cleaved half-transporter bands (non–cross-linked, ~50 kDa). Cross-linked

protein was subsequently used for biochemical assays and EM sample preparation as described below.

ATPase Assays. Measurements of ATP hydrolysis were performed using a molybdate base colorimetric assay as previously described (51). Protein concentrations used in the assays in the range of 0.1–0.2 mg/mL zosuquidar (Medkoo Biosciences) and taxol/paclitaxel (Sigma) were dissolved in DMSO and added to reaction mixes at the desired concentrations. The reactions were started upon addition of 2 mM ATP in the presence of 10 mM $MgCl_2$ at 37 °C. For K_m determination, a range of ATP concentrations was used. Linear regression and statistical analyses were performed using GraphPad Prism 6.

Antibody-Binding Assay. Purified Avi-tagged proteins were first desalted into biotinylation buffer [75 mM NaCl, 25 mM Hepes (pH 7.5), 10 mM magnesium acetate, 10 mM ATP, and 50 μM biotin] containing the detergent/CHS mix used for protein purification before addition of 5–10 μg biotin ligase BirA (produced in-house), and the reaction was allowed to proceed overnight at 4 °C, followed by desalting into buffer containing 150 mM NaCl, 25 mM Hepes (pH 7.5), 10–20% glycerol (buffer A), and the respective detergent/CHS mix. A total of 1–5 pmol of biotinylated proteins was added to each well of a preblocked 96-well Neutravidin plate (Thermo Fisher Scientific) for up to 1 h at room temperature. All incubations were carried out on a plate shaker (Unimax 1010 Orbital Platform shaker; Heidolph) at 350 rpm. Unbound transporters were discarded, and the wells were washed three times with 200 μL of buffer A supplemented with the respective detergent/CHS mix (buffer AD). A total of 100 μL of serially diluted UIC2 antibody was added to the wells and incubated for 30 min at room temperature. Unbound UIC2 was discarded, and the wells were washed three times with buffer AD as before. Horseradish peroxidase (100 μL)-conjugated goat mouse anti-IgG (catalog no. A16072; Thermo Fisher Scientific) diluted to 1 mg/mL (1:1,500) in buffer A was added to the wells for 30 min. After discarding unbound antibodies, the wells were washed as before, followed by development using the TMB Substrate Kit (Thermo Fisher Scientific). Absorbance (450 nM) was read using a BioTek Synergy HT plate reader. Readings were plotted against UIC2 concentrations and fit to a single-site specific binding equation in GraphPad Prism 6. Data were normalized to calculated B_{max} values for comparative purposes.

EM Sample Preparation. LMNG/CHS-purified $ABCB1_{HM}$ constructs were mixed with a two- to threefold molar excess of UIC2-Fab. The $ABCB1_{HM\text{-}EQ}$–UIC2 complex was mixed with a 1:10 wt/wt excess of amphipol A8-35 (Anatrace) for 4 h at 4 °C, followed by overnight biobead (BB-SM2)-mediated removal of detergent. UIC2–Fab complexes of detergent-purified and amphipol-reconstituted samples were concentrated to 5–8 mg/mL before being purified on a $G4000_{SWXL}$ SEC column in buffer containing 250 mM NaCl and 20 mM Tris (pH 8.0) (amphipol) or 150 mM NaCl and 25 mM Hepes (pH 7.5) (detergent samples). Peak fractions corresponding to the purified complexes were pooled and used for cryo-EM grid preparation. For the zosuquidar complex, the inhibitor was added to a final concentration of 10 μM before grid preparation. Freshly purified samples were applied to glow-discharged Lacey carbon grids (LC200; Electron Microscopy Sciences) and plunge-frozen in liquid nitrogen-cooled liquid ethane using a Vitrobot Mark IV (FEI) operated at 4 °C with a blotting time of 3–4 s and >90% humidity.

Data Collection and Processing. An overall data processing scheme for structure determination is provided in *SI Appendix*, Fig. S9. Two different microscopes were used for data collection for the detergent-purified, cross-linked samples and the amphipol-reconstituted samples (FEI Titan Krios 1 and 2, respectively; *SI Appendix*, Table S1). Grids were clipped for loading into a Titan Krios microscope (FEI) running at 300 kV equipped with a Gatan Quantum-LS Energy Filter (GIF) and a Gatan K2 Summit direct electron detector. For the zosuquidar complex of $ABCB1_{HM\text{-}X}$–UIC2, image stacks comprising 48 frames were collected at a nominal magnification of 165,000× in superresolution mode with an estimated dose per frame of 1.54 electrons per square angstrom, corresponding to a total dose of 74 electrons per square angstrom. Stacks were motion-corrected, dose-weighted, and twofold Fourier-cropped to a calibrated pixel size of 0.84 Å in MotionCor2 (52). Contrast transfer function (CTF) estimates were performed using gCTF (53), followed by particle picking and extraction of a total of 469,224 particles from 2,479 micrographs in Relion 2.0 (54–56). After several rounds of 2D classification, 352,880 particles in all usable classes were used for 3D classification using a low-pass-filtered map of the cross-linked apo structure (discussed below) as a reference. Of those, two near-identically looking classes comprising 231,969 (66%) particles were combined and used for 3D refinement and postprocessing to yield a 3D map at 3.78 Å resolution, whereas the remaining particles fell into unusable classes with missing NBDs. We suspect this arises from poorly averaged or heterogeneous particle sets, as well as missing orientation views and the fact that despite high cross-linking efficiency, a subset of transporters may not be linked, and may thus add to overall variability in conformational mobility of the NBDs. A model map for the detergent belt was generated from this map in UCSF Chimera (57), masked in Relion, and used for signal subtraction from the input set of particles used for the initial refinement to yield a final postprocessed map resolution of 3.58 Å. The reported resolution for all maps was based on the FSC cutoff criterion of 0.143 (58). Local resolution estimation was performed using ResMap (59).

For the apo $ABCB1_{HM\text{-}X}$–UIC2 sample, image stacks comprising 80 frames each with an estimated dose per frame of ∼0.9 electrons per square angstrom, corresponding to a total accumulated dose of 72 electrons per square angstrom, were collected at a magnification of 105,000× in superresolution mode, followed by motion correction and dose weighting in MotionCor2. Stacks were twofold binned via Fourier-cropping to a calibrated pixel size of 1.387 Å for processing using Relion 2.0. CTF estimates were performed using gCTF, followed by picking and extraction of a total of 820,566 particles from 2,614 micrographs in Relion. After 2D classification, an input set of 785,152 particles was used for 3D classification using a low-pass-filtered map of the $ABCB1_{HM\text{-}EQ}$–UIC2 structure (discussed below) as a reference. Of those, 517,053 particles (66%) from two similar-looking 3D classes were combined for a round of 3D refinement that yielded a 4.78-Å map. After masking and postprocessing in Relion using automatically determined B-factors, we obtained a resolution of 4.33 Å. This map was used to obtain a model map for the detergent belt, which was generated as described for the zosuquidar complex dataset and used for signal subtraction using the input particle set used for the initial refinement. The new signal-subtracted dataset was then used to refine a single 3D class comprising 517,053 particles. Masking and postprocessing using automatically determined B-factors as before yielded a final map with a resolution of 4.14 Å (map 1) that was used for model building. A second, smaller detergent belt model was similarly generated to create a second signal-subtracted dataset that served as input for one more round of 3D classification, where a search for three 3D classes yielded two distinct classes that shared a similar architecture but showed differences in conformations of TM4 and TM10. Class 1 (153,652 particles) and class 2 (158,827 particles), containing kinked and straight conformations of TM4 and TM10, respectively, were both refined to a resolution of ∼4.5 Å (map 2 and map 3, respectively). The remaining particles fell into the third class containing blurred density in the regions of TM4 and TM10 and were not analyzed further.

For the $ABCB1_{HM\text{-}EQ}$–UIC2 complex, image stacks comprising 80 frames each were collected at a nominal magnification of 105,000× in superresolution mode with an estimated dose per frame of 1.0 electron per square angstrom, corresponding to a total dose of 80 electrons per square angstrom. The software suite Focus (60) was used for online data processing and pruning, applying motion correction with MotionCor2, including twofold binning of the recorded micrographs after motion correction to a calibrated pixel size of 1.336 Å and CTF estimation with gCTF. Particles were picked with gAUTOMATCH (61) using a template-based approach, with templates created from the published ABCB1–UIC2 complex structure (29) using e2proc2d.py (EMAN2) (62). The same model was used later as a starting model in 3D classification. Micrographs were imported for processing in Relion, and a total of 347,049 particles were extracted from 2,038 micrographs, followed by two rounds of 2D classification, to yield a particle set of 112,196 particles. Following two rounds of 3D classification, the remaining 78,282 particles were used for 3D auto-refinement in Relion. Partial signal subtraction was performed to remove the amphipol belt for final 3D refinement and postprocessing to yield a final resolution of 6.25 Å.

Model Building and Refinement. Postprocessed maps, as well as non–B-factor sharpened maps were used for model building in Coot (63) for all datasets. The quality of electron density in the TMD regions of the apo and zosuquidar maps allowed for de novo model building. The map quality in the NBD region was, on average, of lower quality compared with the TMDs, which were resolved to near-atomic resolution (*SI Appendix*, Figs. S4 and S7). Modeling of the NBD region was therefore guided by published structures of ABCB1 [Protein Data Bank (PDB) ID codes 4M1M and 5KO2], followed by manual adjustment where required and permitted by map quality. The UIC2 crystal structure (PDB ID code 5JUE) was manually docked into the Fab density using UCSF Chimera, followed by adjustment in Coot. Two molecules of zosuquidar were unambiguously fit into the corresponding electron density in the ABCB1-binding pocket. We observed electron density characteristic for a bound phospholipid that was tentatively modeled as phosphatidylethanolamine (PE) in both the apo- and zosuquidar-bound occluded $ABCB1_{HM\text{-}X}$ structures.

PE and glycan monomers were obtained from the Coot monomer library (monomer codes 3PE and NAG, respectively). Geometric restraints for all ligands were generated in Phenix. The model for $ABCB1_{HM\text{-}EQ}$–UIC2 was based on the structure of the apo-occluded state. Map quality allowed for rebuilding the TMDs to fit the density and was guided, in part, by the structure of mouse ABCB1 (4M1M).

Real-space refinement of the models was carried out in Phenix (64, 65), with default restraint parameterization along and automatically generated secondary structure restraints. Refinement statistics for all models are presented in *SI Appendix*, Table S1. For validation of the zosuquidar complex model, random coordinate errors up to 0.3 Å were introduced into the refined model, which was subsequently refined against one of the half-maps from the 3D auto-refine run from Relion. Minimal differences in FSCs computed between the refined model and the half-map used for refinement compared with those between the refined model and the half-map excluded from refinement point to a model free from overrefinement (*SI Appendix*, Fig. S3). All figures were prepared using UCSF Chimera and PyMOL (The PyMOL Molecular Graphics System, Version 1.8; Schrödinger, LLC). Cavity volumes were calculated using HOLLOW (66) as described. Structure alignment and rmsd calculations were done in PyMOL. Ligand interaction diagrams were prepared in LigPlot+ (67). Residue numbers in figures are based on equivalent residues in the fully human protein.

ACKNOWLEDGMENTS. We thank the staff at the Scientific Center for Optical and Electron Microscopy at ETH Zürich, especially Peter Tittman, as well as Kenneth N. Goldie and Ariane Fecteau-LeFebvre from Center for Cellular Imaging and Nano Analytics for help with EM data collection. We also acknowledge Bernadette Prinz for help with protein expression and cell culture work. This research was supported by a European Molecular Biology Organization long-term postdoctoral fellowship (to A.A.), National Institutes of Health Grant P20 GM 109091 (to E.V.B.), grants from the Swiss Cancer League (to K.P.L.), and the Swiss National Science Foundation through National Center of Competence in Research Structural Biology and TransCure.

1. Borst P, Schinkel AH (2013) P-glycoprotein ABCB1: A major player in drug handling by mammals. *J Clin Invest* 123:4131–4133.
2. Borst P, Elferink RO (2002) Mammalian ABC transporters in health and disease. *Annu Rev Biochem* 71:537–592.
3. Fromm MF (2004) Importance of P-glycoprotein at blood-tissue barriers. *Trends Pharmacol Sci* 25:423–429.
4. Hillgren KM, et al.; International Transporter Consortium (2013) Emerging transporters of clinical importance: An update from the International Transporter Consortium. *Clin Pharmacol Ther* 94:52–63.
5. Löscher W, Potschka H (2005) Drug resistance in brain diseases and the role of drug efflux transporters. *Nat Rev Neurosci* 6:591–602.
6. Sarkadi B, Homolya L, Szakács G, Váradi A (2006) Human multidrug resistance ABCB and ABCG transporters: Participation in a chemoimmunity defense system. *Physiol Rev* 86:1179–1236.
7. Gottesman MM, Fojo T, Bates SE (2002) Multidrug resistance in cancer: Role of ATP-dependent transporters. *Nat Rev Cancer* 2:48–58.
8. Goda K, et al. (2007) Complete inhibition of P-glycoprotein by simultaneous treatment with a distinct class of modulators and the UIC2 monoclonal antibody. *J Pharmacol Exp Ther* 320:81–88.
9. Mechetner EB, Roninson IB (1992) Efficient inhibition of P-glycoprotein-mediated multidrug resistance with a monoclonal antibody. *Proc Natl Acad Sci USA* 89: 5824–5828.
10. Druley TE, Stein WD, Roninson IB (2001) Analysis of MDR1 P-glycoprotein conformational changes in permeabilized cells using differential immunoreactivity. *Biochemistry* 40:4312–4322.
11. Mechetner EB, et al. (1997) P-glycoprotein function involves conformational transitions detectable by differential immunoreactivity. *Proc Natl Acad Sci USA* 94: 12908–12913.
12. Esser L, Shukla S, Zhou F, Ambudkar SV, Xia D (2016) Crystal structure of the antigen-binding fragment of a monoclonal antibody specific for the multidrug-resistance-linked ABC transporter human P-glycoprotein. *Acta Crystallogr F Struct Biol Commun* 72:636–641.
13. Frank GA, et al. (2016) Cryo-EM analysis of the conformational landscape of human P-glycoprotein (ABCB1) during its catalytic cycle. *Mol Pharmacol* 90:35–41.
14. Aller SG, et al. (2009) Structure of P-glycoprotein reveals a molecular basis for poly-specific drug binding. *Science* 323:1718–1722.
15. Li J, Jaimes KF, Aller SG (2014) Refined structures of mouse P-glycoprotein. *Protein Sci* 23:34–46.
16. Jin MS, Oldham ML, Zhang Q, Chen J (2012) Crystal structure of the multidrug transporter P-glycoprotein from Caenorhabditis elegans. *Nature* 490:566–569.
17. Nicklisch SC, et al. (2016) Global marine pollutants inhibit P-glycoprotein: Environmental levels, inhibitory effects, and cocrystal structure. *Sci Adv* 2:e1600001.
18. Esser L, et al. (2017) Structures of the multidrug transporter P-glycoprotein reveal asymmetric ATP binding and the mechanism of polyspecificity. *J Biol Chem* 292: 446–461.
19. Fox E, Bates SE (2007) Tariquidar (XR9576): A P-glycoprotein drug efflux pump inhibitor. *Expert Rev Anticancer Ther* 7:447–459.
20. Dantzig AH, et al. (1996) Reversal of P-glycoprotein-mediated multidrug resistance by a potent cyclopropyldibenzosuberane modulator, LY335979. *Cancer Res* 56: 4171–4179.
21. Dash RP, Jayachandra Babu R, Srinivas NR (2017) Therapeutic potential and utility of elacridar with respect to P-glycoprotein inhibition: An insight from the published in vitro, preclinical and clinical studies. *Eur J Drug Metab Pharmacokinet* 42:915–933.
22. Robey RW, Massey PR, Amiri-Kordestani L, Bates SE (2010) ABC transporters: Unvalidated therapeutic targets in cancer and the CNS. *Anticancer Agents Med Chem* 10: 625–633.
23. Beck WT, et al. (1996) Methods to detect P-glycoprotein-associated multidrug resistance in patients' tumors: Consensus recommendations. *Cancer Res* 56:3010–3020.
24. Shukla S, Abel B, Chufan EE, Ambudkar SV (2017) Effect of detergent micelle environment on P-glycoprotein (ABCB1)-ligand interactions. *J Biol Chem* 292:7066–7076.
25. Korkhov VM, Mireku SA, Locher KP (2012) Structure of AMP-PNP-bound vitamin B12 transporter BtuCD-F. *Nature* 490:367–372.
26. Hohl M, et al. (2014) Structural basis for allosteric cross-talk between the asymmetric nucleotide binding sites of a heterodimeric ABC exporter. *Proc Natl Acad Sci USA* 111: 11025–11030.
27. Loo TW, Clarke DM (2016) P-glycoprotein ATPase activity requires lipids to activate a switch at the first transmission interface. *Biochem Biophys Res Commun* 472:379–383.
28. Hohl M, Briand C, Grütter MG, Seeger MA (2012) Crystal structure of a heterodimeric ABC transporter in its inward-facing conformation. *Nat Struct Mol Biol* 19:395–402.
29. Carrier I, Julien M, Gros P (2003) Analysis of catalytic carboxylate mutants E552Q and E1197Q suggests asymmetric ATP hydrolysis by the two nucleotide-binding domains of P-glycoprotein. *Biochemistry* 42:12875–12885.
30. Nöll A, et al. (2017) Crystal structure and mechanistic basis of a functional homolog of the antigen transporter TAP. *Proc Natl Acad Sci USA* 114:E438–E447.
31. Verhalen B, et al. (2017) Energy transduction and alternating access of the mammalian ABC transporter P-glycoprotein. *Nature* 543:738–741.
32. Dawson RJ, Locher KP (2006) Structure of a bacterial multidrug ABC transporter. *Nature* 443:180–185.
33. Ritchie TK, Kwon H, Atkins WM (2011) Conformational analysis of human ATP-binding cassette transporter ABCB1 in lipid nanodiscs and inhibition by the antibodies MRK16 and UIC2. *J Biol Chem* 286:39489–39496.
34. Choudhury HG, et al. (2014) Structure of an antibacterial peptide ATP-binding cassette transporter in a novel outward occluded state. *Proc Natl Acad Sci USA* 111: 9145–9150.
35. Zhang Z, Liu F, Chen J (2017) Conformational changes of CFTR upon phosphorylation and ATP binding. *Cell* 170:483–491.e8.
36. Locher KP (2016) Mechanistic diversity in ATP-binding cassette (ABC) transporters. *Nat Struct Mol Biol* 23:487–493.
37. Chufan EE, Kapoor K, Ambudkar SV (2016) Drug-protein hydrogen bonds govern the inhibition of the ATP hydrolysis of the multidrug transporter P-glycoprotein. *Biochem Pharmacol* 101:40–53.
38. Loo TW, Clarke DM (2015) Mapping the binding site of the inhibitor tariquidar that stabilizes the first transmembrane domain of P-glycoprotein. *J Biol Chem* 290: 29389–29401.
39. Pajeva IK, et al. (2013) Interactions of the multidrug resistance modulators tariquidar and elacridar and their analogues with P-glycoprotein. *ChemMedChem* 8:1701–1713.
40. Loo TW, Clarke DM (2008) Mutational analysis of ABC proteins. *Arch Biochem Biophys* 476:51–64.
41. Loo TW, Clarke DM (1998) Mutational analysis of human P-glycoprotein. *Methods Enzymol* 292:480–492.
42. Chufan EE, et al. (2013) Multiple transport-active binding sites are available for a single substrate on human P-glycoprotein (ABCB1). *PLoS One* 8:e82463.
43. Szewczyk P, et al. (2015) Snapshots of ligand entry, malleable binding and induced helical movement in P-glycoprotein. *Acta Crystallogr D Biol Crystallogr* 71:732–741.
44. Loo TW, Bartlett MC, Clarke DM (2003) Permanent activation of the human P-glycoprotein by covalent modification of a residue in the drug-binding site. *J Biol Chem* 278:20449–20452.
45. Loo TW, Bartlett MC, Clarke DM (2003) Simultaneous binding of two different drugs in the binding pocket of the human multidrug resistance P-glycoprotein. *J Biol Chem* 278:39706–39710.
46. Loo TW, Bartlett MC, Clarke DM (2003) Substrate-induced conformational changes in the transmembrane segments of human P-glycoprotein. Direct evidence for the substrate-induced fit mechanism for drug binding. *J Biol Chem* 278:13603–13606.
47. Johnson ZL, Chen J (2017) Structural basis of substrate recognition by the multidrug resistance protein MRP1. *Cell* 168:1075–1085.e9.
48. Srinivasan V, Pierik AJ, Lill R (2014) Crystal structures of nucleotide-free and glutathione-bound mitochondrial ABC transporter Atm1. *Science* 343:1137–1140.
49. Backliwal G, Hildinger M, Chenuet S, Dejesus M, Wurm FM (2008) Coexpression of acidic fibroblast growth factor enhances specific productivity and antibody titers in transiently transfected HEK293 cells. *N Biotechnol* 25:162–166.
50. Nguyen TA, et al. (2015) Functional anatomy of the human microprocessor. *Cell* 161: 1374–1387.
51. Chifflet S, Torriglia A, Chiesa R, Tolosa S (1988) A method for the determination of inorganic phosphate in the presence of labile organic phosphate and high concentrations of protein: Application to lens ATPases. *Anal Biochem* 168:1–4.

52. Zheng SQ, et al. (2017) MotionCor2: Anisotropic correction of beam-induced motion for improved cryo-electron microscopy. *Nat Methods* 14:331–332.
53. Zhang K (2016) Gctf: Real-time CTF determination and correction. *J Struct Biol* 193:1–12.
54. Scheres SH (2012) RELION: Implementation of a Bayesian approach to cryo-EM structure determination. *J Struct Biol* 180:519–530.
55. Scheres SH (2012) A Bayesian view on cryo-EM structure determination. *J Mol Biol* 415:406–418.
56. Kimanius D, Forsberg BO, Scheres SH, Lindahl E (2016) Accelerated cryo-EM structure determination with parallelisation using GPUs in RELION-2. *eLife* 5:e18722.
57. Pettersen EF, et al. (2004) UCSF Chimera–A visualization system for exploratory research and analysis. *J Comput Chem* 25:1605–1612.
58. Scheres SH, Chen S (2012) Prevention of overfitting in cryo-EM structure determination. *Nat Methods* 9:853–854.
59. Kucukelbir A, Sigworth FJ, Tagare HD (2014) Quantifying the local resolution of cryo-EM density maps. *Nat Methods* 11:63–65.
60. Biyani N, et al. (2017) Focus: The interface between data collection and data processing in cryo-EM. *J Struct Biol* 198:124–133.
61. Urnavicius L, et al. (2015) The structure of the dynactin complex and its interaction with dynein. *Science* 347:1441–1446.
62. Tang G, et al. (2007) EMAN2: An extensible image processing suite for electron microscopy. *J Struct Biol* 157:38–46.
63. Emsley P, Lohkamp B, Scott WG, Cowtan K (2010) Features and development of Coot. *Acta Crystallogr D Biol Crystallogr* 66:486–501.
64. Brown A, et al. (2015) Tools for macromolecular model building and refinement into electron cryo-microscopy reconstructions. *Acta Crystallogr D Biol Crystallogr* 71: 136–153.
65. Adams PD, et al. (2010) PHENIX: A comprehensive Python-based system for macromolecular structure solution. *Acta Crystallogr D Biol Crystallogr* 66:213–221.
66. Ho BK, Gruswitz F (2008) HOLLOW: Generating accurate representations of channel and interior surfaces in molecular structures. *BMC Struct Biol* 8:49.
67. Laskowski RA, Swindells MB (2011) LigPlot+: Multiple ligand-protein interaction diagrams for drug discovery. *J Chem Inf Model* 51:2778–2786.